Energy &
Environmental
Science

ROYAL SOCIETY
OF CHEMISTRY

PAPER

Cite this: *Energy Environ. Sci.*, 2022, **15**, 4659

Demonstration of 10+ hour energy storage with ϕ1″ laboratory size solid oxide iron–air batteries†

Qiming Tang,[a] Yongliang Zhang,[a] Nansheng Xu,[a] Xueling Lei *[b] and Kevin Huang *[a]

Received 19th May 2022,
Accepted 30th August 2022

DOI: 10.1039/d2ee01626e

rsc.li/ees

Long duration electricity storage (LDES) with 10+ hour cycle duration is an economically competitive strategy to accelerate the penetration of renewable energy into the utility market. Unfortunately, none of the available energy storage technologies can meet the LDES requirements in terms of duration and cost. The newly emerged solid-oxide iron–air batteries (SOIABs) with energy-dense solid iron as an energy storage material have inherent advantages for LDES applications. Herein, we report for the first time the LDES capability of SOIABs even at a laboratory scale. We show that SOIABs with an Ir-catalyzed Fe-bed can achieve excellent energy density (625 W h kg^{-1}), long cycle duration (12.5 h) and high round-trip efficiency (∼90%) under LDES-related working conditions. Given the excellent low-rate performance and the use of earth-abundant, low-cost Fe as an energy storage material, we conclude that the SOIAB is a well-suited battery technology for LDES applications.

Broader context

Cost-effective, large-scale stationary electricity storage systems play a key role in achieving resilient grid stability and accelerating renewable energy penetration into the utility market. Recent analyses suggest that long-duration electricity storage (LDES) with multi-day storage and even seasonal energy arbitrage will have a significant impact on the commercial deployment of low-cost wind and solar powers. Unfortunately, as of today, no commercial energy storage technologies are available to fulfill the LDES requirements. For example, today's most dominant large-scale electricity storage technologies (*e.g.*, pumped-hydro storage (PHS)) can only store up to 10 hours of energy, which only satisfies applications of daily baseload energy time-shift and cannot leverage the full benefits of LDES. Conventional Li-ion batteries are also severely limited in extending storage durations beyond 10 hours due to the high costs to scale up, not to mention the safety concern on using clustered Li-ion battery systems. Redox flow batteries are scalable and safe, but their low energy density and efficiency have constrained their applications in LDES. Therefore, there is a significant lack of viable LDES technologies in the utility market. Here in this work, we demonstrate that a laboratory size solid oxide iron–air battery can readily achieve long-duration cycles with high energy density and round-trip efficiency. By scaling up the overall size of the SOIAB system, the energy storage capability can be extended to weeks, months or even the entire renewable-rich season.

1. Introduction

Cost-effective, large-scale stationary electricity storage systems play a critical role in achieving resilient grid stability and accelerating renewable energy penetration into the utility market. Recent analyses suggest that long-duration electricity storage (LDES) with multi-day storage and even seasonal energy arbitrage will have significant advantages in promoting deeper penetration of low-cost wind and solar powers.[1–6] As of today, most commercial electricity storage deployments, as well as research and development, focus primarily on systems with durations ≤10 hours at rated power.[7,8] For example, today's most dominant large-scale electricity storage technologies (*e.g.*, pumped-hydro storage (PHS)) can only store up to 10 hours of energy, which only satisfies applications of daily baseload energy time-shift and cannot leverage the full benefits of LDES. Conventional Li-ion batteries are also severely limited in extending storage durations beyond 10 hours due to the high costs to scale up, not to mention the safety concern on using clustered Li-ion battery systems. Redox flow batteries are scalable and safe, but their low energy density and efficiency have also constrained their applications in LDES. Therefore, there is a significant lack of viable LDES technologies in the utility market.

To address this technological gap, the author's group has recently developed a new type of all solid-state battery operated on oxide-ion chemistry, *viz.* a solid-oxide iron–air battery

---

[a] *Department of Mechanical Engineering, University of South Carolina, Columbia, SC 29201, USA. E-mail: huang46@cec.sc.edu*

[b] *Department of Physics, Jiangxi Normal University, Nanchang, Jiangxi 330022, China. E-mail: xueling@mail.ustc.edu.cn*

† Electronic supplementary information (ESI) available. See DOI: https://doi.org/10.1039/d2ee01626e

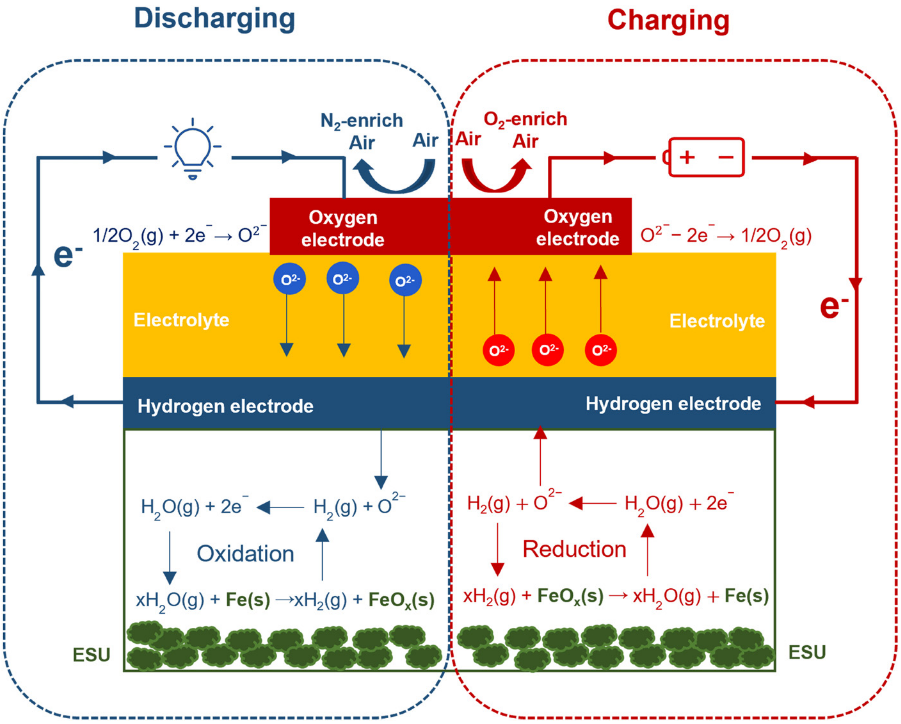

Fig. 1 Schematic of the working principle of the all-solid oxide Fe–air battery.

(SOIAB), in which the chemical energy of oxygen transported in the form of O^{2-} is reversibly stored in an energy-dense Fe/FeO_x-bed (or abbreviated as ''Fe-bed'' throughout this article) that is integrated within the anode chamber of a reversible solid oxide cell (RSOC).[9–12] Fig. 1 schematically shows the SOIAB consisting of an RSOC and an Fe-bed or the Energy Storage Unit (ESU). In this battery design, the oxygen electrode (OE) and hydrogen electrode (HE) are open to air of an unlimited oxygen source and enclosed in a low-cost Fe-bed chamber, respectively. During cycling, the RSOC alternately operates in fuel cell mode during the discharge process and in electrolyzer mode during the charge process, while oxygen is being transferred *via* a gas-phase H_2/H_2O shuttle and stored within the Fe-bed *via* the Fe–O redox reaction. One unique feature of the SOIAB is its free access to oxygen in air (thus no oxygen storage is needed for the OE), making it easy for LDES applications.[9]

Realizing the durability and cost issues for conventional high-temperature (700–800 °C) RSOCs, our early research effort on SOIABs has mainly focused on developing key enabling materials for intermediate temperature (IT) 500–600 °C operation. During the development, we realized that while the durability of the IT-SOIAB can be significantly improved at the IT, its rate performance is limited by the higher electrode overpotentials and more sluggish FeO_x reduction kinetics. For example, a 550 °C-SOIAB can cycle at a low rate (*e.g.* 0.2C or 10 mA cm^{-2} for a 1.4 cm^2 cell) and low Fe-utilization (U_{Fe} = 3.1% of 0.01 mole Fe loading) for 150 hours (or 500 cycles) without any noticeable degradation, but it degrades much faster at higher C-rates and U_{Fe}.[9,13] SOIAB's low rate-performance, while not suitable for applications requiring fast charge and discharge cycles, might not necessarily be a problem for LDES if there is enough Fe available in the battery to store energy (electricity equivalent to O^{2-}). For example, a simple calculation based on Faraday's law indicates that 67.3 kg of Fe is needed to store electricity for 24 hours at a current of 100 A and Fe-utilization (U_{Fe}) of 20% (see Fig. S1a and b in the ESI†). Since Fe-mass exclusively determines the energy capacity of an SOIAB, we will use Fe-mass in the Fe-bed to express the specific energy densities achieved under different conditions for comparison purpose in this work. It should also be a good estimate of the energy storage capacity that a practical SOIAB system can offer since LDES applications are stationary and the total weight of the system plays a minor role.

It is also interesting to note that energy (size of Fe-bed) and power (area of the electrode) can be separately pursued in SOIAB systems for user-specific applications. We can envision that a large Fe-bed can sustain electricity storage for months or even the entire renewable-rich season in the low power mode. We also acknowledge that the charging process (electrolysis) is endothermic, which could influence temperature uniformity across the battery. However, like any high temperature solid oxide electrolytic cells, by operating the cell voltage at near thermoneutral potential, the need for extra heat to keep the temperature constant can be mitigated. For SOIABs, this thermoneutral potential is 1.40 V at 550 °C, which falls well within the operating voltage range. Therefore, in addition to many other advantages of Fe-bed materials (*e.g.*, earth abundance and low cost), it is reasonable to deem IT-SOIABs a potential technology for LDES.

From our early work, we have identified two major problems that limit the overall performance of a SOIAB: (1) Fe-bed's sluggish FeO_x-to-Fe reduction kinetics[14] and (2) RSOC's high electrode overpotentials.[9] To address these issues, we have previously shown that the synthesis of nanostructured Fe-bed materials[11] and the addition of catalyst (*e.g.*, Pd) nanoparticles can boost the FeO_x-to-Fe reduction kinetics.[9] However, our effort to further improve RSOC's electrochemical performance has been very limited in the past.

Here we report our recent effort in improving the performance of the components in an SOIAB. We first show how OE, electrolyte thickness, and HE impact the RSOC's performance by using a three-electrode symmetrical cell combined with DC-biased electrochemical impedance spectroscopy (EIS) methodology. The obtained overpotential (η) *vs.* current density (j) relationship of the OE under both fuel cell and electrolyzer modes is then combined with the V–j curve of a full cell to separate the individual contribution from the OE, electrolyte, and HE. We then show how the performance (specific energy density, round-trip efficiency (RTE) and cycle life) of the SOIAB is affected by C-rate and U_{Fe}. We also show how the Ir catalyst in the Fe-based ESU boosts the charging (FeO_x reduction) performance of the SOIAB at both low and high U_{Fe}. Finally, by combining an improved RSOC with the Ir-catalyzed Fe-bed, we demonstrate the LDES performance with multiple stable 12.5 hour charge/discharge cycles on an ϕ1″ size SOIAB.

2. Results and discussion

2.1. Cell microstructure and composition

A detailed description of the fabrication process is provided in the Experimental section. The cross-sectional view of the microstructure of the baseline HE-supported cell fabricated using the dip-coating method is shown in Fig. 2(a), where a 10 μm thick, dense ScSZ electrolyte and a 10 μm thick, porous HE functional layer are clearly seen deposited on the HE-support (∼400 μm thick). Fig. 2(b) shows the microstructure of the HE-support with a pore size in the range of 3–5 μm after reduction in H_2-3% H_2O at 550 °C. For the best performing RSOC with 2 wt% gadolinium-doped ceria (GDC) infiltrated HE-support (to be shown later), Fig. 2(c) shows a similar after-reduction microstructure to that in Fig. 2(b), but the infiltrated GDC appears to be present as a thin layer on the Ni-ScSZ surface (see the insert in Fig. 2(c)). The microstructures of the OE/electrolyte interface before and during testing for 250 hours under 0.2C and 550 °C are shown in Fig. S2 (ESI†). No significant change was found.

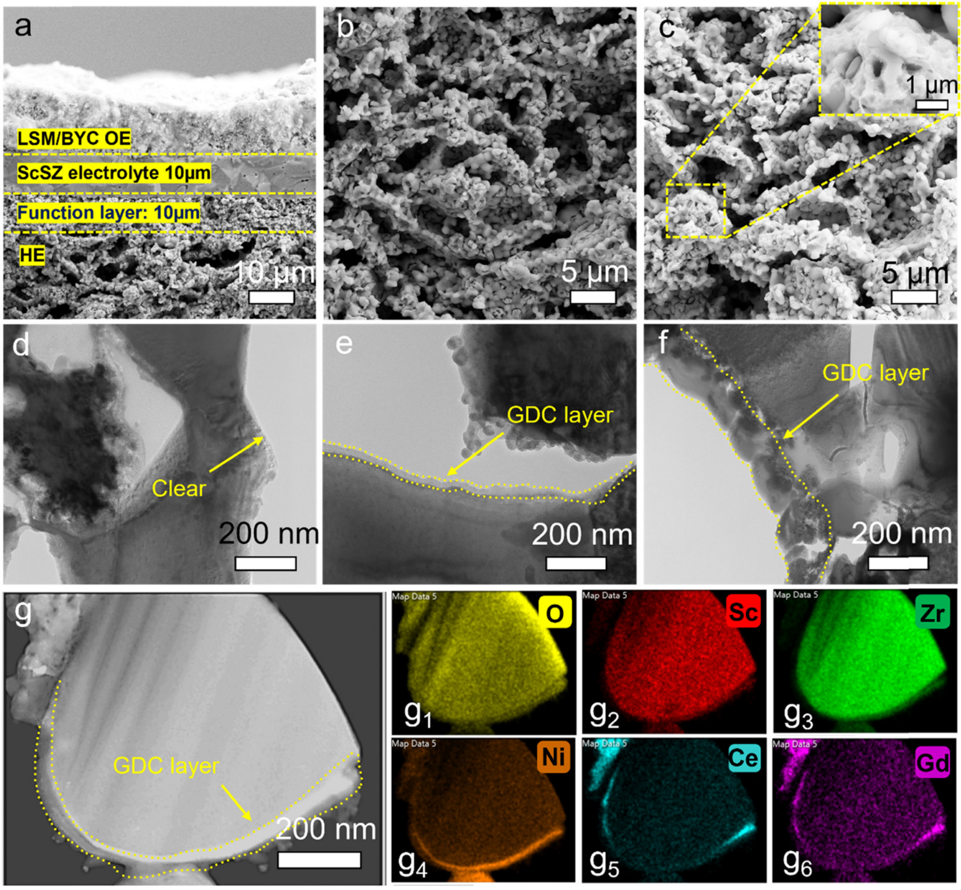

Fig. 2 (a) Cross-sectional SEM micrographs of the fabricated pre-reduction HE-supported cell by dip-coating; (b) HE microstructure after H_2-reduction; (c) 2 wt% GDC infiltrated HE microstructure; (d) TEM images of the baseline HE-supported cell; (e) HE-support with 2 wt% GDC; (f) HE-support with 4 wt% GDC; (g) STEM mapping of a HE particle with 2 wt% GDC after testing.

To further examine the morphology of the GDC infiltrant, we performed STEM on the GDC layer. While there is no GDC present in the baseline HE, Fig. 2(d) and (e) show a roughly 20 nm thick GDC layer on the surface of ScSZ/NiO particles for the 2 wt% GDC sample, while it is thicker (~40–80 nm) for the 4 wt% GDC sample (see Fig. 2(f) and Fig. S3–S5, ESI†). The HE with 2 wt% GDC was further analyzed after testing for 500 hours. Fig. 2(g) shows the STEM image of an ScSZ particle coated with a ~20 nm thick GDC and a Ni layer. Both GDC samples with Ni phases play an active catalytic role in promoting H_2 oxidation and H_2O reduction reactions during cycling. The elemental mapping in Fig. 2(g1)–(g6) provides an expected uniform distribution of Zr, Sc, O, Ni, Ce and Gd around an ScSZ particle; their semiquantitative contents analyzed by SEM-EDS are given in Fig. S6 (ESI†), which further confirms the STEM-EDS results.

2.2. Fe-bed morphology and composition

The chemical compositions of the Fe-bed material, *i.e.* Fe_2O_3/ZrO_2 (the use of ZrO_2 is to mitigate Fe particle sintering) and IrO_2 impregnated Fe_2O_3/ZrO_2 composites were determined by XRD; the results are shown in Fig. S7 (ESI†). The pristine Fe_2O_3/ZrO_2 powders show peaks at $2\theta = 24$, 33.2, 25.6, 40.8, 49.5 and 54.1°, which are assigned to the (012), (104), (110), (113), (024) and (116) planes of Fe_2O_3 (PDF # 33-0664). The peaks at $2\theta = 28.1°$ and 35.1° can be indexed to the $(\bar{1}11)$ and (002) planes of ZrO_2, respectively. The sharp peaks free of any other impurity phase suggest high crystallinity and purity of the sample. After introducing IrO_2, no new peaks can be observed. However, its intensity and shape of the peak appear to be weaker and broader, implying relatively low crystallinity of IrO_2 particles in the sample. In addition, metallic Fe and ZrO_2 are found in the cycled Fe_3O_4/ZrO_2–Ir sample, suggesting that the iron oxide has been fully reduced to iron.

The morphology of the pristine Fe_2O_3/ZrO_2 powder is shown in SEM images of Fig. 3(a); a slight agglomeration is observed, which is not surprising given the thermal treatment of the powder after the synthesis. After adding IrO_2, Fig. 3(b) shows that Fe_2O_3/ZrO_2 particles are covered with discrete IrO_2 nanoparticles (NPs) in a size of ~5 nm (see Fig. 3(c) and Fig. S8, ESI†). In addition, the high-resolution TEM (HRTEM) image of Fig. 3(c) indicates crystalline fringes matching well to Fe_2O_3, ZrO_2 and IrO_2, *i.e.*, 0.51, 0.31, 0.36, 0.27 and 0.23 nm corresponding to the (100) and $(\bar{1}11)$ planes of ZrO_2, (110) and (104) planes of Fe_2O_3, and the (200) plane of IrO_2, respectively. The IrO_2 NPs uniformly distributed on the surface of Fe_2O_3 are expected to provide catalytic sites for H_2 "spillover".[15–17]

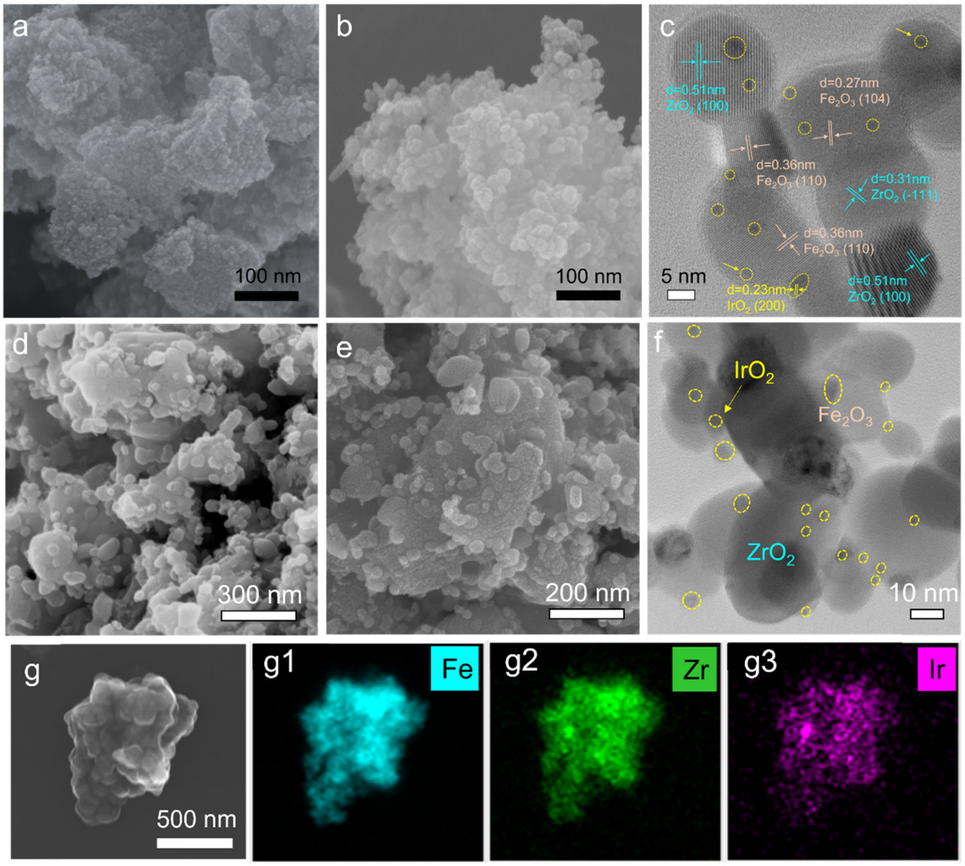

Fig. 3 Characterization of the Fe-bed materials: (a) SEM image of fresh Fe_2O_3/ZrO_2; (b) SEM image of fresh Fe_2O_3/ZrO_2–IrO_2; (c) HRTEM image of fresh Fe_2O_3/ZrO_2–IrO_2; (d) SEM image of Fe_3O_4/ZrO_2 after 100 h of testing; (e) SEM image of Fe_3O_4/ZrO_2–Ir after 100 h of testing; (f) HRTEM image of Fe_3O_4/ZrO_2–Ir after 100 h of testing; (g) elemental mapping of Fe_3O_4/ZrO_2–Ir after 100 h of testing: (g1) Fe, (g2) Zr, (g3) Ir. Note that Fe_2O_3 and IrO_2 turned to Fe_3O_4/Fe and Ir, respectively, after testing.

After testing at 550 °C for hundreds of hours, all particles in Fe_2O_3/ZrO_2 without IrO_2 grew from 50 to 200 nm as expected (see Fig. 3(d)). Similarly, Fig. 3(e) shows that the IrO_2-added Fe_2O_3/ZrO_2 exhibits similar morphologies, but the HRTEM image of Fig. 3(f) suggests that Ir particles (IrO_2 becomes Ir during and after testing) remain relatively unchanged, still spreading uniformly over ZrO_2 and Fe particles. The elemental mapping of Fig. 3(g) further confirms that Fe, Zr and Ir dispense uniformly within the Fe-bed and there is no apparent Fe accumulation/separation on the surface as observed previously after multiple redox cycles at 750 °C.[18] The presence of inert ZrO_2 and low operating temperature are clearly the reason for retaining such chemical homogeneity.[19,20]

2.3. Evaluation of electrode overpotential of RSOC

To understand which RSOC component limits the overall performance, we apply the symmetrical three-electrode cell (STEC) method we developed recently to the OE.[21] Fig. 4(a) and (b) show a schematic of the STEC method. The counter electrode (CE) and the working electrode (WE) are the identical OE of LSM-BYC, while the reference electrode (RE) is a silver wire/Au paste attached to the circumference of the electrolyte disk. Depending on the direction of the DC current applied, the EIS spectrum related to either ORR (discharge) or OER (charge) polarization can be obtained. For example, when a positive current density (j) is applied as shown in Fig. 4(b), the obtained EIS spectrum of the OE as a WE is related to the OER process. Fig. S9 (ESI†) shows the obtained polarization resistance (R_p) of both ORR and OER *vs.* j at 550–700 °C. R_p is observed to decrease with j, which is expected from the Butler–Volmer equation. The degree of R_p reduction is more pronounced at lower temperatures, implying the low-temperature dominance of the charge transfer process. At higher temperatures where the charge-transfer process is more facile, j has less effect on R_p. It is interesting to mention that OER-R_p of the LSM-BYC becomes noticeably lower than that of the ORR at high j, making the polarization curve asymmetrical. This finding is important evidence that LSM-BYC is a better OER electrode than the ORR electrode at high j. The R_p stability of the LSM-BYC OE was also evaluated at j = 10 mA cm^{-2} and 550 °C; the results are shown in Fig. S10a–c (ESI†). The LSM-BYC electrode shows good stability for both OER and ORR polarization over ~500 h (it is *de facto* decreasing with time during the polarization), implying that any degradation in the performance of the RSOC may be related to either the HE or the electrolyte.

The obtained $R_p(j)$–j data in Fig. S9 (ESI†) are further integrated to produce overpotential $\eta(j)$ by

$$\eta(j) = \int_0^j R_p \mathrm{d}j \tag{1}$$

The overpotential (η) derived from R_p *vs.* j is shown in Fig. 4(c). A typical Tafel curve in both OER and ORR domains is clearly

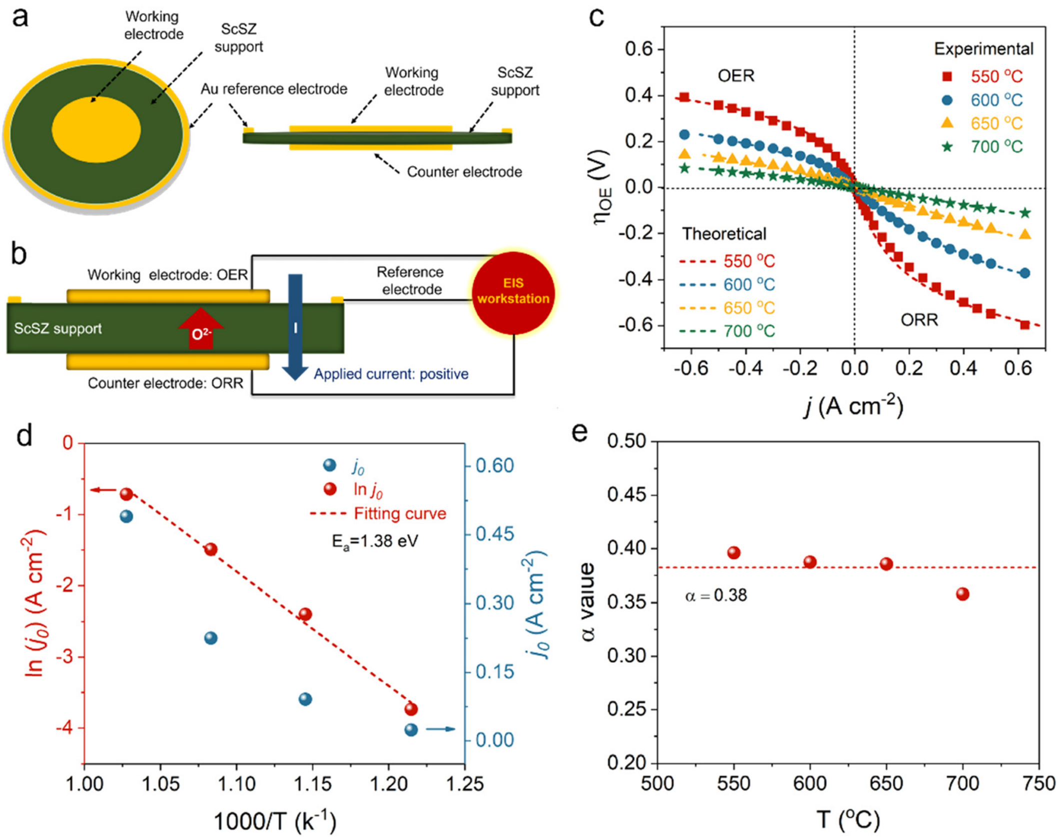

Fig. 4 (a and b) Schematic of the STEC method; (c) η_{OE} *vs.* j; (d) ln(j_0) *vs.* 1/T and α *vs.* T.

observed. We further apply the below Butler–Volmer equation (assuming that the ORR and the OER are multi-step charge transfer processes, but the rate-limiting step involves single electron transfer) to fit the data with exchange current density j_0 and transfer coefficient α as variables:[22]

$$j = j_\mathrm{o}\left(\exp\left(\frac{-\alpha F\eta}{RT}\right) - \exp\left(\frac{(1-\alpha)F\eta}{RT}\right)\right) \qquad (2)$$

where F, R and T have their usual meanings. The results are shown in Fig. 4(d) and (e) as a function of temperature. Clearly, j_0 follows the Arrhenius relationship with the activation energy E_a = 1.38 eV, while α is insensitive to T and averaged to be ~0.38 over 550–700 °C.

With η_OE in Fig. 4(c) and combining the overall V–j curve from the full cell, the anode overpotential η_HE can be separated by the following equations

$$\eta_\mathrm{t} = \pm(E_\mathrm{N} - E_\mathrm{C}) \qquad (3)$$

$$\eta_\mathrm{HE} = \eta_\mathrm{t} - (\eta_\mathrm{ohm} + \eta_\mathrm{OE}) \qquad (4)$$

where η_t is the total overpotential; "+" for the ORR and "−" for the OER; $\eta_\mathrm{ohm} = jR_\mathrm{o}$, where R_o is the ohmic resistance obtained from EIS; E_C and E_N are the cell voltage of the full cell and Nernst potential, respectively.

Fig. 5(a) shows a typical discharge and charge profile of the battery at j = 10 mA cm^{-2} (0.2C) and U_Fe = 5%. Based on the profile and eqn (3), η_t of discharge and charge processes is obtained separately. The results in Fig. 5(a) suggest a slightly higher η_t for discharge than that of the charge, which is consistent with the observation of higher R_p for the ORR (discharge) than that of the OER (charge) shown in Fig. S9 (ESI†). After separating η contributions from the cell components, Fig. 5(b) and (c) compare them among cell components for the baseline cell and the GDC-modified cell. Without GDC in the HE, η_HE accounts for 67% and 59% for the discharge and charge, respectively. In contrast, the percentages drop to 43.8 and 17% for 2 wt% GDC-added HE. This comparison illustrates the dominance of HE in the overall performance of the baseline battery. Fig. 5(d) plots the effect of GDC loading on η_HE, suggesting that 2 wt% is the optimal GDC loading. For η_HE with other GDC loadings, refer to Fig. S11 (ESI†). The optimal GDC loading at 2 wt% is understood to be the result of balanced reactive sites between GDC and Ni phase. In other words, too much GDC may cover and block more active Ni particles for the reactions. The improved RSOC performance is also illustrated in Fig. S12 and S13 (ESI†).

2.4. Electrochemical performance evaluation of SOIAB

Fig. 6(a) shows the voltage profiles *vs.* time during the cycle at different C rates varying from 0.1C (5 mA cm^{-2}) to 1.5C

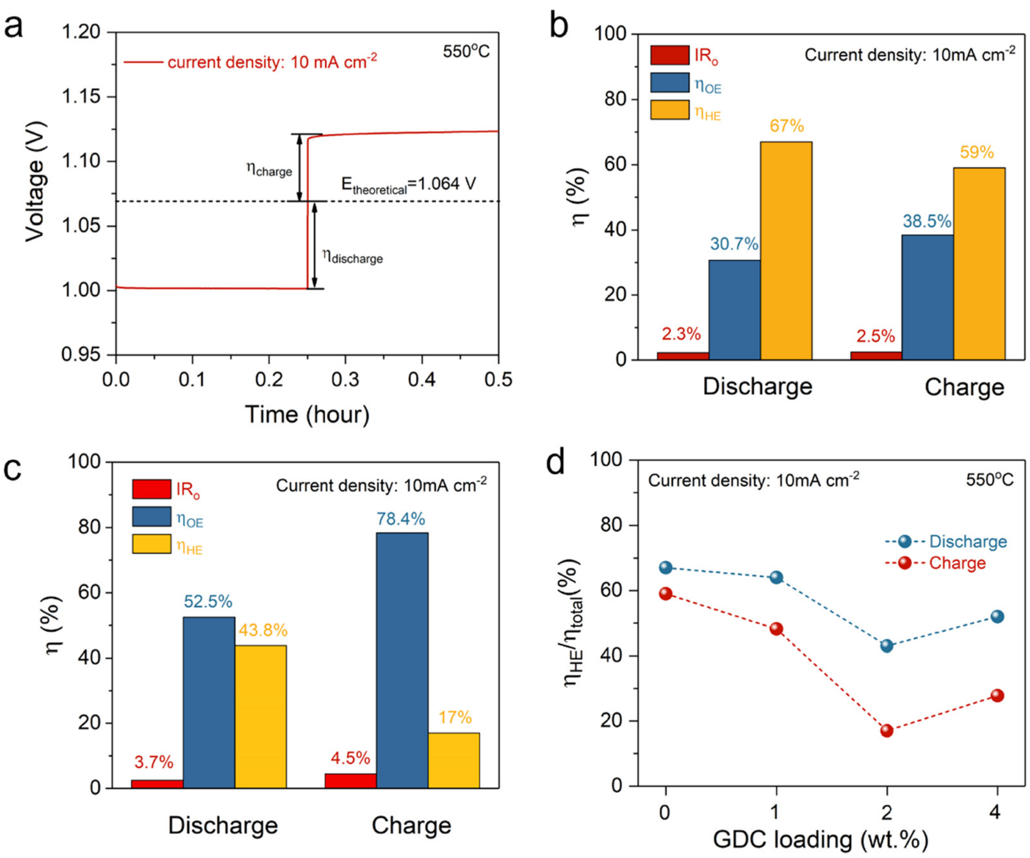

Fig. 5 (a) A typical discharge and charge profile of SOIAB at j = 10 mA cm^{-2} with U_Fe = 5% of a baseline cell; (b) η distribution among different cell components of the baseline cell; (c) η distribution among different cell components of the 2 wt% GDC-modified cell; (d) η contribution from the HE for different GDC loadings.

(75 mA cm^{-2}) but a fixed U_{Fe} = 10% for both baseline and IrO_2-added batteries (containing 0.001 mol active Fe); the corresponding RTE calculated is shown in Fig. 6(b). As expected, the battery's RTE decreases with C-rate, varying from 96% at 0.1C to 63.9% at 1.5C for the IrO_2-battery. In contrast, the baseline battery already exhibits a lower RTE = 58% at 0.6C (j = 25 mA cm^{-2}). The introduction of IrO_2 clearly improves the C-rate performance, particularly during the charging cycle by boosting the FeO_x-reduction kinetics. When the C-rate returns to 0.1C, a high RTE = 95.2% is still achievable.

The U_{Fe} influences SOIAB's RTE and energy density. Fig. 6(c) shows voltage profiles at different U_{Fe} under a fixed j = 10 mA cm^{-2} (0.2C). As U_{Fe} is increased from 5 to 100%, the total discharge time is increased proportionally from 15 to 300 min; see the ESI† for the calculation. In this study, only one cycle at each U_{Fe} was performed to show the effect of U_{Fe} on specific energy density. The low and high cutoff voltages were set to 0.6 and 2.0 V for the discharge and charge cycle, respectively. From the results shown in Fig. 6(c), it is evident that the IrO_2-battery can be cycled with a stable voltage plateau even at U_{Fe} = 100%. However, the discharge voltage of the baseline battery experiences a sharp decrease and reaches the cutoff voltage quickly after $U_{Fe} > 80\%$, implying a severe mass transport limitation, likely caused by the depletion of Fe due to the insufficient reduction of FeO_x during the charging cycle.

The discharge and charge specific energy density (SED) and RTE are further calculated from Fig. 6(c) and plotted in Fig. 6(d) as a function of U_{Fe}. With an increase of U_{Fe}, both discharge and charge SEDs (based on Fe mass in the Fe-bed) increase, achieving the discharge SED (DSED) of 63.8, 254, 631 and 1248 W h kg^{-1}-Fe at U_{Fe} of 5, 20, 50 and 100%, respectively. The deviation between the theoretical and experimental values increases with U_{Fe}, which reflects the mass transport limitation. It should also be noted that RTE is only deceased by ∼5% (from 93.6 to 89.3%) as U_{Fe} is increased from 5 to 100%. Overall, the introduction of IrO_2 into Fe_2O_3/ZrO_2 has not only significantly improved the C-rate performance but also enabled the battery to operate at higher U_{Fe}.

2.5. Long-term stability at different U_{Fe} of SOIAB

The long-term stability of the baseline and IrO_2-SOIAB at 0.2C (j = 10 mA cm^{-2}) and U_{Fe} = 5% was first tested and the results are compared in Fig. 7(a). The IrO_2-SOIAB exhibits a slightly lower charging voltage and marginally better stability than the baseline battery under low U_{Fe} and C-rate conditions. The corresponding discharge and charge SEDs, (DSED and CSED, respectively) of the IrO_2-battery are shown in Fig. 7(b), indicating DSED = 63.2 W h kg^{-1}-Fe, CSED = 69.2 W h kg^{-1}-Fe and RTE = 91.3% at U_{Fe} = 5% after 500 cycles (0.25 h per cycle duration). Fig. S14 (ESI†) shows the baseline SOIAB with similar

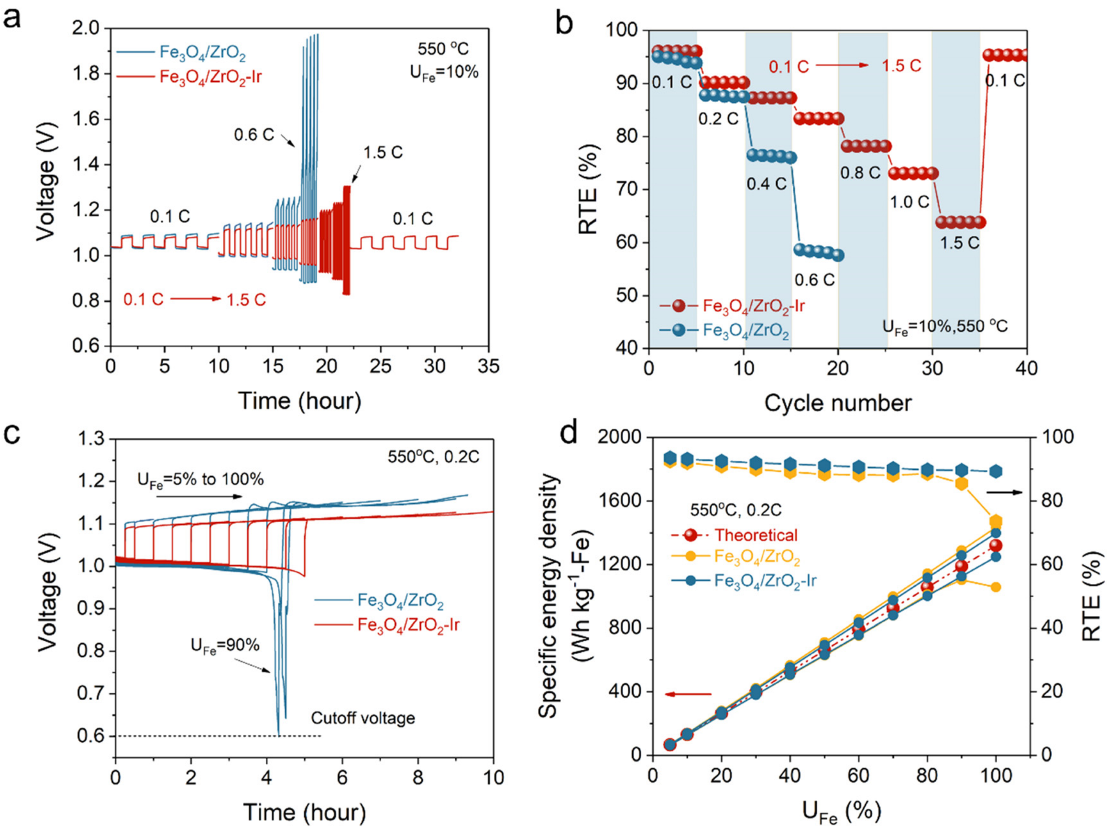

Fig. 6 Electrochemical performance of baseline and IrO_2-battery. (a) Voltage profile *vs.* time during the cycle at different C rates; (b) effect of C-rate on RTE; (c) voltage profiles *vs.* time at a fixed j = 10 mA cm^{-2} (0.2C) and different U_{Fe} (5–100%); (d) discharge and charge SED and the corresponding RTE *vs.* U_{Fe}.

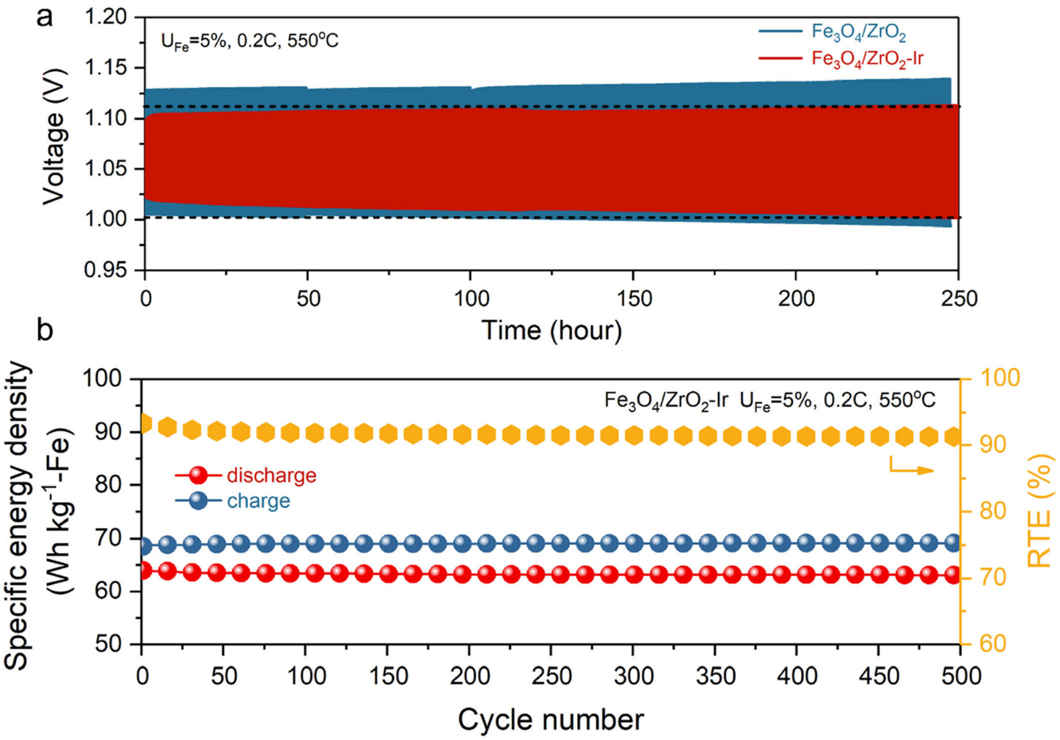

Fig. 7 (a) Comparison of cycle stability of SOIAB with different ESU materials; (b) the corresponding SED and RTE of SOIAB with Fe_3O_4/ZrO_2–Ir ESU materials operated at U_{Fe} = 5% and 0.2C.

performance, *e.g.*, DSED = 62.0 W h kg^{-1}-Fe, CSED = 69.0 W h kg^{-1}-Fe, and RTE = 90% after 250 cycles. While under low U_{Fe}, both baseline and IrO_2 batteries show a similar long-term performance, their stability and RTE at a high U_{Fe} are more meaningful for practical applications since LDES requires large energy capacity, which can be achieved by operating at high U_{Fe}.

We, therefore, performed a comparative long-term test on both baseline and IrO_2-batteies at U_{Fe} = 50% and 0.2C (j = 10 mA cm^{-2}). Fig. 8(a) compares cyclic voltage profiles of the two cells. The baseline cell clearly exhibits pronounced degradation under this condition, failed at charging where the voltage hit 2.0 V (the high cutoff voltage) after 80 hours. This is likely because the kinetic rate of Fe-oxide reduction (charging process) is insufficient to match up the charging current density due to the thicker FeO_x layer formed under high U_{Fe}. In contrast, the cyclic voltage is much more stable for the IrO_2-battery. Interestingly, the cell eventually hit 0.8 V (the low cutoff voltage) during discharge after 200 hours. The fact that the IrO_2-cell exhibits stable charging voltage and declining discharging voltage during 200 hour cycling implies that the oxidation of Fe becomes rate limited, which is understandable given that the FeO_x reduction kinetics has been effectively boosted by the IrO_2 catalyst. During the stable performance of 200 hours (or 40 cycles of 2.5 hour per cycle), the IrO_2-battery exhibits a DSED of 617.6 W h kg^{-1}-Fe at RTE = 87.4% under U_{Fe} = 50% and j = 10 mA cm^{-2} (0.2C), much better than the

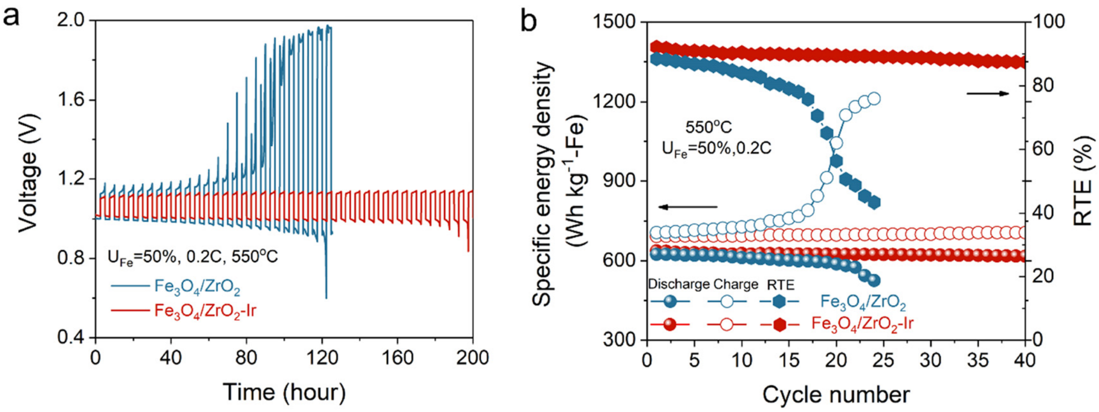

Fig. 8 Battery performance tested at U_{Fe} = 50% and 0.2C for different ESU materials: (a) voltage profiles; (b) SED and RTE *vs.* cycle number.

baseline cell (see Fig. 8(b)). Overall, compared to the previously published results, the IrO_2-battery represents a significant improvement in capacity, RTE and cycle stability.[9–11,13,23,24] Therefore, using a small amount of expensive IrO_2 in the Fe-bed is justified for the SOIAB. To increase the cycle duration for practical LDES application, the mass of the Fe-bed needs to be increased accordingly as shown in Fig. S1b (ESI†). Obviously, greater amount of the Fe-bed requires a larger anode chamber, which ultimately increases the size of the ROSC and the magnitude of charge/discharge current densities.

To truly demonstrate SOIAB's LDES capability, we further assembled an SOIAB with more Fe-mass (in this case 0.28 g or 0.005 mol) in the Fe-bed. This is the maximum amount of Fe we can pack within the ϕ1″ cell without H_2/H_2O gas transport limitation. This amount of Fe-mass enables a cycle duration of 12.5 h at 10 mA cm^{-2} (0.04C for this scaled-up battery) and U_{Fe} = 50%. The measured voltage profiles are shown in Fig. 9(a). Translating Fig. 9(a) into battery performance, Fig. 9(b) shows that an RTE of ~90% has been achieved with a high DSED of 625 W h kg^{-1}-Fe. This level of performance demonstrates a great potential of the SOIAB for LDES applications, even with a lab-size SOIAB. More important to practical applications, a simple multiplication (n) of Fe-mass used in this work will result in a cycle duration greater than 12.5 hours as the size of the SOIAB is increased correspondingly.

Despite the promising LDES performance, SOIABs still face engineering challenges in demonstrating commercially meaningful durability and self-discharge rate, both of which are closely tied to the current development of solid oxide cells (SOCs) for power and hydrogen productions. For example, the self-discharge rate of SOIABs is determined by the gas tightness of SOCs, which is also a high standard for SOC operations. The same argument can be applied to the durability concern. Therefore, as SOC's engineering advances toward commercialization, so will SOIABs.

2.6. Understanding the mechanism of IrO_2-catalyzed Fe-oxide reduction kinetics

IrO_2 has been known as an excellent catalyst for many chemical reactions.[25–27] In the context of H_2 reduction, IrO_2 will be reduced to Ir, which acts as a catalyst to H_2 spillover. To better understand the fundamental catalysis effect of introducing Ir, density functional theory (DFT) calculations were performed to elucidate how Ir catalyzes H_2 reduction in the formation of Fe_3O_4. Details on the calculation method and structure of Fe_3O_4 can be found in the Experimental section and Fig. S15 (ESI†).

Fig. 10(a) shows that on the pure Fe_3O_4 surface, the relative energy for H_2 dissociative adsorption (or spillover) on the $Fe_3O_4(111)$ surface (H_2-ads) is −4.62 eV. After dissociation, one H atom needs to overcome 0.78 eV energy barrier (−4.62 eV *vs.* −3.84 eV) to migrate to the adjacent O atom on the surface, while another H bonds with the adjacent Fe atom, to reach the first transition state 1 (TS1). However, further breaking of the Fe–H bond to allow the H atom to migrate toward the O atom for H_2O formation requires a much higher 1.16 eV energy barrier (−4.46 eV *vs.* −3.48 eV), to reach transition state 2 (TS2).

In the Fe_3O_4–Ir case, however, two Fe–O bonds are found broken, leading to O protrusion out of the surface and formation of a new elongated Fe–O bond (see Fig. 10(b) and Fig. S16, ESI†). Comparatively, the energy for H_2 spillover on the surface of the Ir atom (H_2-dis) is lower (−4.93 eV) than that in the pure Fe_3O_4-case (−4.62 eV), suggesting the catalytic effect of Ir on H_2 spillover. While the energy level to reach TS1 is not significantly different for both cases, there is a considerable difference in the FS1 energy. For the Fe_3O_4–Ir case, the final FS1 energy is −6.08 eV, decreased from −4.15 eV at TS1, while there is only a slight decrease from −3.84 (TS1) eV to −4.64 eV (FS1) for the pure Fe_3O_4 case.

The final step of H-migration, from FS1 to FS2, with two H atoms separately adsorbed to the O atom of the Fe_3O_4–Ir surface, which is equivalent to 0.40 eV energy barrier (−6.08 eV *vs.* −5.68 eV), significantly lower than that of the pure Fe_3O_4 case (1.16 eV). Therefore, it is concluded that the presence of Ir can greatly promote H-migration and breaking of Fe–O bonds, leading to a boosted reduction kinetics of Fe_3O_4.

Corresponding to the DFT model, we also sketch Fig. 10(c) to illustrate physically the pathways of the FeO_x reduction process in the presence of an Ir catalyst, which includes surface H_2 spillover on Ir and migration of the activated H atoms from an Ir nanoparticle onto the FeO_x lattice.

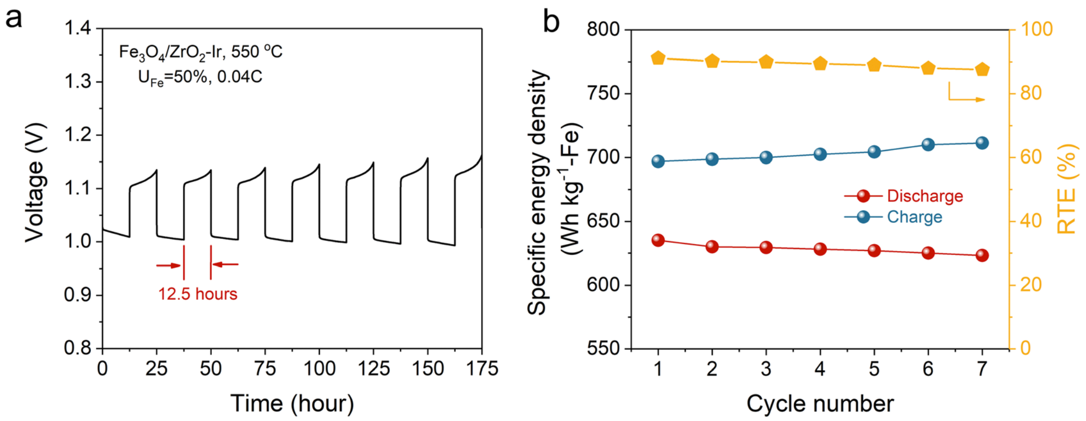

Fig. 9 The charge–discharge performance of the SOIAB (a single cell with 0.28 g active Fe mass, enabling 12.5 h of cycle duration at 10 mA cm^{-2} and U_{Fe} = 50%): (a) voltage profiles; (b) corresponding SED and RTE *vs.* cycle number.

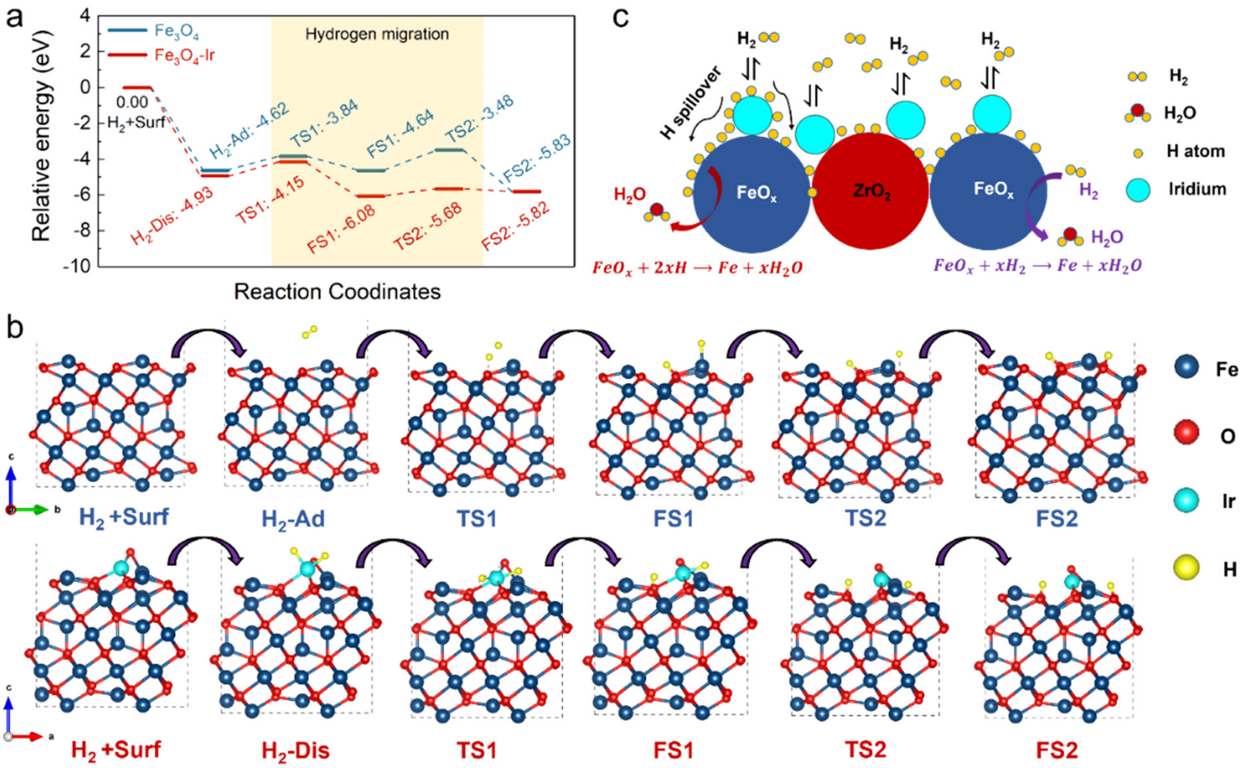

Fig. 10 (a) Calculated energetics of initial, transition (TS) and final states (FS) for H_2 dissociative adsorption and migration on Fe_3O_4(111) and Fe_3O_4–Ir(111) surfaces. (b) The optimized H_2 dissociative adsorption and migration of structures on the Fe_3O_4(111) surface with/out Ir. (c) A schematic representation of pathways in the Fe_3O_4/ZrO_2–Ir reduction process.

The lowered activation energy of Fe-oxide reduction by Ir is indeed experimentally observed by Temperature Programmed Reduction (TPR). Fig. 11(a) shows the TPR profiles of the baseline and Ir-added samples. The baseline sample exhibits three reduction peaks located at 297.2, 472.9 and 605.6 °C, which can be assigned to the reduction of Fe_2O_3 to Fe_3O_4, Fe_3O_4 to FeO and FeO to Fe, respectively. After adding Ir into Fe_2O_3/ZrO_2, only one Fe-oxide reduction peak is observed at 461.1 °C, signaling a significantly improved reaction kinetics.

To quantify the reduction kinetics, we applied the Kissinger method[28] to extract the activation energy of the reduction process. From the peak temperature, $T_{\max}$, of a TPR profile, the following relationship can be drawn:

$$\ln\left(\frac{\Phi}{{T_{\max}}^2}\right) = -\frac{E_a}{RT_{\max}} + \ln\left(\frac{AR}{E}\right) + C \qquad (5)$$

where Φ is the ramping rate; E_a is the activation energy of the reduction process; C is the constant; A is the pre-exponential term; R is the universal gas constant. Since E_a is a constant for a fixed thermal process, by plotting $\ln\left(\frac{\Phi}{{T_{\max}}^2}\right)$ *vs.* $\frac{1}{T_{\max}}$, the slope $(-E_a/R)$ can be obtained from the Arrhenius plot.

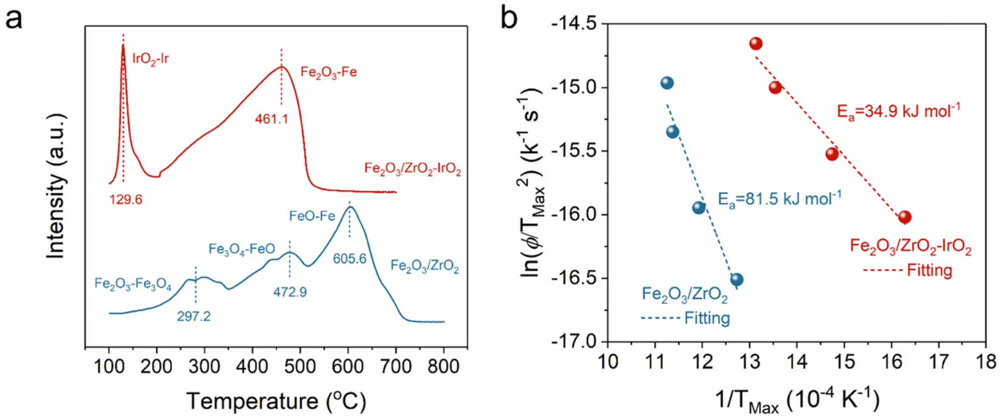

Fig. 11 (a) TPR profiles of baseline and IrO_2-added samples at a ramping rate of 10 °C min^{-1}; (b) Arrhenius plots of $\frac{\Phi}{{T_{\max}}^2}$.

Fig. 11(b) shows the Arrhenius plots of the two samples, from which the activation energy E_a for the baseline and Ir-added samples is calculated as 81.5 and 34.9 kJ mol^{-1}, respectively, suggesting that IrO_2 significantly lowers the energy barrier for FeO_x-reduction kinetics. Fig. S17 (ESI†) shows the original TPR profiles at different ramping rates from 2.5 to 15 °C min^{-1}.

3. Conclusion

In summary, this study demonstrated a SOIAB with significantly improved energy storage performance with long cycle duration, moving this new battery technology a step closer to practical LDES applications. The improvement in the storage performance was realized through optimizations in the electrolyte, electrodes, and energy storage materials. The use of three electrode configuration allows us to pinpoint the overpotential contribution from the OE, through which the overpotential contributions from other cell components are deconvoluted as a function of current density after combining with the cell voltage, ohmic resistance and Nernst potential of a full battery. The finding is that the HE contributes a majority of overpotential to the total cell voltage loss. Adding the GDC catalyst into the HE substrate appreciably lowers the overpotential of the HE, thus improving the battery cell performance. In the meanwhile, after introducing Ir nanoparticles into the Fe-based ESU, the slow Fe_3O_4 reduction kinetics related to the charging process has been significantly boosted. We show computationally that Ir can drastically lower energy barriers for H_2 spillover and breaking of Fe–O bonds, thus promoting the Fe_3O_4 reduction kinetics. With all the improvements made in battery materials, we finally demonstrate multiple 12.5 h cycles with high DSED (625 W h kg^{-1}-Fe) and RTE (87%). Overall, given the excellent low C-rate performance and low-cost Fe, it is reasonable to consider SOIABs as a LDES-compatible device. With the scaled-up SOIAB systems, achieving electricity storage with 10+ hour, daily, weekly, monthly and even seasonal cycle is expected.

4. Experimental section

4.1. Synthesis of materials

4.1.1 Fe-bed ESU materials. The starting baseline Fe-bed (the energy storage material) is a mixture of Fe_2O_3 and ZrO_2. During operation in a SOIAB, Fe_2O_3 is first reduced to metallic Fe, on which Fe/Fe_3O_4 becomes the active redox couple to regular oxygen transported through the RSOC during charge/discharge cycles. The fresh baseline Fe_2O_3/ZrO_2 mixture was prepared using a co-precipitation method. Briefly, the stoichiometric solutions of $Fe(NO)_3 \cdot 9H_2O$ (≥99.999%, Sigma-Aldrich) and $ZrO(NO)_2 \cdot xH_2O$ (≥99.999%, Alfa-Aesar) in a molar ratio of Fe : Zr = 85 : 15 were first dissolved in deionized water separately. Then the two solutions were mixed in a beaker with a cation concentration of 0.1 M. The resultant clear orange solution was then added dropwise to an $(NH_4)_2CO_3$ (Sigma-Aldrich) solution bath with constant stirring. To ensure full precipitation of all cations in the solution, the molar ratio of $(NH_4)_2CO_3$ and M^{n+} (M = Zr and Fe) was kept as $n(NH_4)_2CO_3 : nM^{n+} = 2.0 : 1$. The resultant brownish precipitate was then left in the solution for 20 h with continuous stirring. Finally, the aged suspension was filtered and washed several times with ethanol, dried overnight at 80 °C and calcined in air at 600 °C for 5 h to yield the Fe_2O_3/ZrO_2 product.

To obtain the IrO_2 impregnated Fe_2O_3/ZrO_2, the as-prepared Fe_2O_3/ZrO_2 was first ball milled using a planetary ball mill (BM4X-04, COL-INT TECH) in a zirconium container for 20 h with a milling speed of 300 rpm. Then, 0.1 g of Ir precursor, iridium III 2,4-pentanedionate ($C_{15}H_{21}IrO_6$, Sigma-Aldrich) dissolved in 2 mL of acetone (99.5%, Sigma-Aldrich) was added into 1 g of milled Fe_2O_3/ZrO_2 powders in an agate mortar followed by mixing and grinding. Finally, the impregnated powders were calcined at 600 °C for 2 h. The total IrO_2 loading in the ESU is around 4 wt% of Fe_2O_3/ZrO_2 mass. During operation, IrO_2 turns into metallic Ir as a catalyst in the Fe-bed of the battery.

4.1.2 $La_{0.8}Sr_{0.2}MnO_3$ (LSM)/$(Bi_{0.75}Y_{0.25})_{0.93}Ce_{0.07}O_{1.5}$ (BYC) OE. The LSM/BYC composite OE was prepared by the combustion method using nitrates as the metal precursors. Briefly, for LSM preparation, stoichiometric amounts of $La(NO_3)_3 \cdot 6H_2O$ (Sigma-Aldrich), $Sr(NO_3)_2$ (Sigma-Aldrich) and $Mn(NO_3)_2 \cdot 4H_2O$ (Sigma-Aldrich) were dissolved into 500 mL of 0.2 M citric acid (CA, Sigma-Aldrich) solution with a molar ratio of metal ions : CA = 1 : 2. Then 10 mL of nitric acid (70%, Sigma-Aldrich) solution was added into the mixture solution by stirring. The pH of the solution was then adjusted to ∼6 with ammonia (28–30%, Sigma-Aldrich). Finally, the transparent solution was heated in an oven at 240 °C until auto-combustion. The obtained powders were then broken up and calcinated at 900 °C for 5 h. The BYC powders were prepared by a similar process with $Bi(NO_3)_3 \cdot 5H_2O$ (Sigma-Aldrich), $Y(NO_3)_3 \cdot 6H_2O$ (Sigma-Aldrich), and $Ce(NO_3)_3 \cdot 6H_2O$ (Sigma-Aldrich) as the metal precursors, except that the molar ratio of the metal ions to CA is 1 : 1.5 and the calcination temperature is 700 °C.

4.2. Fabrication of the HE-supported electrolyte

The HE-substrate was first prepared by the dry-pressing method. Briefly, NiO, ScSZ and carbon powders with a weight ratio of 6 : 4 : 3 were ball-milled for 4 hours in ethanol with ZrO_2 balls. Then the slurry was dried overnight at 80 °C. The dried powders were then fully mixed with 5 wt% PVB in acetone using an agate mortar, followed by pressing into pellets of ϕ1.0″ and partially sintering at 900 °C for 2 h to achieve enough strength. The HE functional layer was deposited by dipping the HE pellet into a slurry containing the NiO : ScSZ = 60 : 40 (wt%) mixture with a 10 wt.% carbon for 15 s. Then, the pellet was pulled out of the suspension and dried in an oven for 10 min. The pellet was subsequently sintered at 800 °C for 2 h, after which a thin layer of the ScSZ electrolyte was deposited on top of the functional layer using the same dip-coating technique. The recipe of the electrolyte slurry is like the functional layer but without NiO. The HE, functional layer and electrolyte triple-layers were finally co-sintered at 1350 °C for 5 h. The final product was ground down to ∼400 μm thickness. The thicknesses of the ScSZ electrolyte and HE functional layer are both ∼10 μm with a diameter of 0.8 inch.

4.3. Infiltrating GDC nanoparticles into the HE substrate

$Gd_{0.2}Ce_{0.8}O_2$ (GDC) nanoparticles were infiltrated into the NiO-ScSZ HE substrate to improve the HE performance. To do so, 0.5 M nitrate solutions of GDC precursors were prepared by dissolving a stoichiometric amount of $Gd(NO_3)_3 \cdot 6H_2O$ (Sigma-Aldrich) and $Ce(NO_3)_3 \cdot 6H_2O$ (Sigma-Aldrich) in distilled water with 20 vol% ethanol. Ethylene diamine tetraacetic acid (EDTA, Sigma-Aldrich) and citric acid (CA, Sigma-Aldrich) as a surfactant and a chelating agent, respectively, were dissolved into diluted ammonia and then the solution was added to the GDC precursor solution. The pH of the solution was carefully adjusted to 8. The molar ratio of CA to EDTA to metal ions was kept at 2 : 1 : 1. Fig. S18 (ESI†) shows the process of HE infiltration along with half-cell fabrication steps. After infiltration, the NiO-ScSZ/ScSZ half-cell was fired in air at 500 °C for 1 h to decompose metal nitrates into their respective oxides. The loading of GDC was controlled by the number of infiltration and determined based on the mass change before and after infiltration.

4.4. Single cell fabrication

Two types of cells were fabricated in this work to examine the battery performance: (i) HE-supported full cell and (ii) electrolyte-supported symmetrical cell. For the HE-supported full cell, the OE was made by screen printing the OE ink on top of the ScSZ electrolyte surface. The ink consists of a mixture of LSM, BYC and a V-006 binder (Columbia International) in a weight ratio of LSM : BYC : V-006 = 40 : 60 : 150. After printing and drying, the cell is calcined at 800 °C for 2 h to make the final cell. The effective surface area of the cathode electrode is 1.4 cm^2, and the silver mesh and gold paste were used as current collectors for both the OE and the HE.

For the electrolyte-supported symmetrical three-electrode cell, the ScSZ electrolyte with the thickness of 200 μm was made using the tape casting method. The same cathode as the full cell was screen-printed symmetrically on both sides of the ScSZ electrolyte and then fired at 800 °C for 2 hours. To make the third reference electrode, a silver wire was wound and fixed by gold paste along the circumference of the electrolyte pellet (see Fig. S19, ESI†).

4.5. Battery cell assembly and testing

For testing a typical battery, the ESU material (0.056 and 0.28 g Fe for short and long-duration cycles) was first sped over an Al_2O_3 wool and then loaded into the chamber of the battery holder layer by layer to ensure minimal mass transport limitation. Then, the RSOC was placed into the grove of the holder with the HE substrate facing down. A layer of glass slurry consisting of glass powder (from Schott GM31107) mixed with the binder was then applied along the perimeter between the cell and the holder. The current collection wires on the HE-side were carefully routed through an insulating glass ring and the glass layer to avoid short circuiting with the metal holder.

The electrochemical performance of the battery was tested using a Solartron Multichannel system (model 1470e) in conjunction with a Solartron 1255 frequency response analyzer. The battery was first heated in air from room temperature to 680 °C and held for 30 min to melt the glass and achieve gas tightness. Then, the temperature was decreased to 550 °C for testing. Besides, 5% H_2/N_2 at 50 $cm^3\ min^{-1}$ was first introduced into the HE-chamber for 50 minutes to purge the residual air and then switched to pure H_2 through a room temperature water bubbler to reduce the HE and Fe-bed into their metallic states. The open-circuit voltage (OCV) of the battery cell was constantly monitored and used to judge the completion of the reduction process. Once it is done, the initial V–j curves and EIS of the RSOC were first measured at OCV under flowing 3% H_2O–H_2. Then the H_2 outlet and inlet valves were closed in sequence, and the OCV was monitored until it reached the theoretical potential of 1.064 V (for Fe–Fe_3O_4 redox couple at 550 °C). Now the battery is ready for discharge/charge cycling. The MultiStat software is used for collecting data and performing data analysis. The rate performance, U_{Fe} and cycle stability were systematically evaluated based on the protocol given in Table S1 (ESI†). The cutoff voltages for discharge and charge are set at 0.6 and 2.0 V, respectively.

4.6. Materials characterization

The phase compositions of the prepared Fe_2O_3/ZrO_2 composite, LSM and BYC were examined by X-ray diffraction operating at a scan rate of 2° min^{-1} from 10 to 80° using Rigaku D/MAX-2100. The morphologies of the Fe-bed materials and battery cell components were examined using a field emission scanning electron microscope (FESEM) (Zeiss Gemini 500) *via* energy dispersive X-ray spectroscopy (EDS) for elemental mapping analysis. A high-resolution transmission electron microscope (HRTEM, HITACHI H-9500) and a scanning transmission electron microscope (STEM, HITACHI SU9000) were also used to examine the infiltrated GDC nanoparticles. The focused-ion-beam technique (FIB, Hitachi NB-5000) was used to prepare TEM samples.

4.7. Computational details

All the calculations were performed using the Vienna *Ab Initio* Simulation Package (VASP) based on the density functional theory (DFT).[29,30] The projector augmented wave approach[31,32] was adopted to describe the interaction of ions and electrons, and the general gradient approximation in the Perdew–Burke–Ernzerhof form was employed for the electronic exchange-correlation functional.[33] In the simulations, Fe_3O_4(111) surfaces with a vacuum width of 22 Å were investigated based on the previous report that shows (111) as the most stable surface.[34] Each (111) surface unit consisted of 12 single layers with tetrahedral Fe termination, in which the atoms of top 3 layers were relaxed, and other 9 layers were fixed in all surface calculations. Spin polarization was considered in all calculations. The cutoff energy for the plane wave basis expansion was set to

500 eV. The structure optimization was obtained until the force on each ion dropped below 0.05 eV $Å^{-1}$ and the energy was smaller than 10^{-4} eV. In this work, the Monkhorst–Pack scheme *k*-points sampling[35] was used for integration in the first Brillouin zone, and the separation of the *k*-point mesh was < 0.03 $Å^{-1}$. The migration energy barrier of H on different surfaces was calculated by locating the transition states, which can be obtained by analyzing the minimum-energy path for the H-diffusion processes using the climbing-image nudged elastic band method. In addition, van der Waals correction was carried out for the interactions between the adsorbed H_2 molecule and the surface. For an accurate treatment of the electron correlation in the localized 3d-Fe orbital, we used rotationally invariant density functional theory, and an effective U_{eff} of 3.8 eV was used to calculate the on-site Coulomb interaction of Fe-3d states.[36]

Conflicts of interest

There are no conflicts to declare.

Acknowledgements

We would like to thank the National Science Foundation for the financial support under award number 1801284 and the Department of Energy, Office Fossil Fuels, National Energy technology Laboratory for the financial support under award number DE-FE-0032111, and the Natural Science Foundation of China (Grant no. 12164020). We also gratefully acknowledge the Hefei Advanced Computing Center for the computational support.

References

1 P. Denholm and M. Hand, *Energy Policy*, 2011, **39**, 1817–1830.
2 W. A. Braff, J. M. Mueller and J. E. Trancik, *Nat. Clim. Change*, 2016, **6**, 964–969.
3 M. R. Shaner, S. J. Davis, N. S. Lewis and K. Caldeira, *Energy Environ. Sci.*, 2018, **11**, 914–925.
4 O. J. Guerra, J. Zhang, J. Eichman, P. Denholm, J. Kurtz and B.-M. Hodge, *Energy Environ. Sci.*, 2020, **13**, 1909–1922.
5 J. A. Dowling, K. Z. Rinaldi, T. H. Ruggles, S. J. Davis, M. Yuan, F. Tong, N. S. Lewis and K. Caldeira, *Joule*, 2020, **4**, 1907–1928.
6 C. A. Hunter, M. M. Penev, E. P. Reznicek, J. Eichman, N. Rustagi and S. F. Baldwin, *Joule*, 2021, **5**, 2077–2101.
7 P. Albertus, J. S. Manser and S. Litzelman, *Joule*, 2020, **4**, 21–32.
8 R. E. Ciez and D. Steingart, *Joule*, 2020, **4**, 597–614.
9 C. Zhang and K. Huang, *ACS Energy Lett.*, 2016, **1**, 1206–1211.
10 X. Zhao, X. Li, Y. Gong, N. Xu and K. Huang, *RSC Adv.*, 2014, **4**, 22621–22624.
11 X. Zhao, X. Li, Y. Gong and K. Huang, *Chem. Commun.*, 2014, **50**, 623–625.
12 X. Zhao, Y. Gong, X. Li, N. Xu and K. Huang, *J. Electrochem. Soc.*, 2013, **160**, A1241–A1247.
13 C. Zhang and K. Huang, *Chem. Commun.*, 2017, **53**, 10564–10567.
14 X. Jin, X. Zhao and K. Huang, *J. Power Sources*, 2015, **280**, 195–204.
15 R. Prins, *Chem. Rev.*, 2012, **112**, 2714–2738.
16 W. Karim, C. Spreafico, A. Kleibert, J. Gobrecht, J. VandeVondele, Y. Ekinci and J. A. van Bokhoven, *Nature*, 2017, **541**, 68–71.
17 M. Xiong, Z. Gao and Y. Qin, *ACS Catal.*, 2021, **11**, 3159–3172.
18 C. Zhang, C. Ji, W. Wang, D. Schmidt, X. Jin, J. P. Lemmon and K. Huang, *Energy Environ. Sci.*, 2016, **9**, 3746–3753.
19 Q. Tang, Y. Ma and K. Huang, *ACS Appl. Energy Mater.*, 2021, **4**, 7091–7100.
20 Q. Tang and K. Huang, *Chem. Eng. J.*, 2022, **434**, 134771.
21 X. Jin and K. Huang, *J. Electrochem. Soc.*, 2020, **167**, 124501.
22 L. R. F. Allen and J. Bard, *Electrochemical Methods: Fundamentals and Applications*, Wiley, 2nd edn, 2001, ISBN: 978-970-471-04372-04370.
23 X. Zhao, Y. Gong, X. Li, N. Xu and K. Huang, *J. Mater. Chem. A*, 2013, **1**, 14858–14861.
24 X. Zhao, X. Li, Y. Gong, N. Xu, K. Romito and K. Huang, *Chem. Commun.*, 2013, **49**, 5357–5359.
25 S. Cherevko, S. Geiger, O. Kasian, N. Kulyk, J.-P. Grote, A. Savan, B. R. Shrestha, S. Merzlikin, B. Breitbach, A. Ludwig and K. J. J. Mayrhofer, *Catal. Today*, 2016, **262**, 170–180.
26 F. Shen, Y. Wang, G. Qian, W. Chen, W. Jiang, L. Luo and S. Yin, *Appl. Catal., B*, 2020, **278**, 119327.
27 J. Ahmed and Y. Mao, *Electrochim. Acta*, 2016, **212**, 686–693.
28 O. J. Wimmers, P. Arnoldy and J. A. Moulijn, *J. Phys. Chem.*, 1986, **90**, 1331–1337.
29 G. Kresse and J. Hafner, *Phys. Rev. B: Condens. Matter Mater. Phys.*, 1993, **47**, 558–561.
30 G. Kresse and J. Furthmüller, *Phys. Rev. B: Condens. Matter Mater. Phys.*, 1996, **54**, 11169–11186.
31 G. Kresse and D. Joubert, *Phys. Rev. B: Condens. Matter Mater. Phys.*, 1999, **59**, 1758–1775.
32 P. E. Blöchl, *Phys. Rev. B: Condens. Matter Mater. Phys.*, 1994, **50**, 17953–17979.
33 J. P. Perdew, K. Burke and M. Ernzerhof, *Phys. Rev. Lett.*, 1996, **77**, 3865–3868.
34 G. J. Martin, R. S. Cutting, D. J. Vaughan and M. C. Warren, *Am. Mineral.*, 2009, **94**, 1341–1350.
35 H. J. Monkhorst and J. D. Pack, *Phys. Rev. B: Solid State*, 1976, **13**, 5188–5192.
36 X. Yu, Y. Li, Y.-W. Li, J. Wang and H. Jiao, *J. Phys. Chem. C*, 2013, **117**, 7648–7655.